Extraction of mechanical properties of materials through deep learning from instrumented indentation

Lu Lu[a,1], Ming Dao[b,1,2], Punit Kumar[c], Upadrasta Ramamurty[c], George Em Karniadakis[a,2], and Subra Suresh[d,2]

[a]Division of Applied Mathematics, Brown University, Providence, RI 02912; [b]Department of Materials Science and Engineering, Massachusetts Institute of Technology, Cambridge, MA 02139; [c]School of Mechanical and Aerospace Engineering, Nanyang Technological University, 639798 Singapore; and [d]Nanyang Technological University, 639798 Singapore

Contributed by Subra Suresh, February 10, 2020 (sent for review December 20, 2019; reviewed by Javier Llorca and Ting Zhu)

Instrumented indentation has been developed and widely utilized as one of the most versatile and practical means of extracting mechanical properties of materials. This method is particularly desirable for those applications where it is difficult to experimentally determine the mechanical properties using stress–strain data obtained from coupon specimens. Such applications include material processing and manufacturing of small and large engineering components and structures involving the following: three-dimensional (3D) printing, thin-film and multilayered structures, and integrated manufacturing of materials for coupled mechanical and functional properties. Here, we utilize the latest developments in neural networks, including a multifidelity approach whereby deep-learning algorithms are trained to extract elastoplastic properties of metals and alloys from instrumented indentation results using multiple datasets for desired levels of improved accuracy. We have established algorithms for solving inverse problems by recourse to single, dual, and multiple indentation and demonstrate that these algorithms significantly outperform traditional brute force computations and function-fitting methods. Moreover, we present several multifidelity approaches specifically for solving the inverse indentation problem which 1) significantly reduce the number of high-fidelity datasets required to achieve a given level of accuracy, 2) utilize known physical and scaling laws to improve training efficiency and accuracy, and 3) integrate simulation and experimental data for training disparate datasets to learn and minimize systematic errors. The predictive capabilities and advantages of these multifidelity methods have been assessed by direct comparisons with experimental results for indentation for different commercial alloys, including two wrought aluminum alloys and several 3D printed titanium alloys.

3D printed materials | stress–strain behavior | multifidelity modeling | transfer learning | machine learning

Instrumented Indentation for Extracting Mechanical Properties of Materials

Instrumented indentation has been a research topic for scientific investigations as well as industrial applications during the past several decades (1–9). Here, the loading force (P) of the indenter tip and the resultant depth of penetration (h) of the tip into the material are continuously recorded both during loading and unloading. Such depth sensing or instrumented indentation has, in recent years, emerged as an appealing means of probing the mechanical properties of hard and soft materials, devices, components, and structures over a wide spectrum of size scales, from nanometers to meters, with sufficient resolution to measure forces over the range of micronewtons to kilonewtons, and displacements over the range of nanometers to centimeters (7, 8). Some key advantages of instrumented indentation as a method to extract properties include the need to test only a relatively small volume of the material (in relation to its overall volume), which for many applications would render it an essentially nondestructive probe. Furthermore, it offers the potential to determine processing-induced residual stresses (2), anisotropic properties (10), property gradients arising from compositional, microstructural, or residual-stress gradients in materials (11, 12), as well as coupled electrical–mechanical responses of integrated systems such as those involving piezoelectric materials (13, 14). It is especially suited for extracting material properties in a wide variety of applications involving additive manufacturing, near–net-shape manufacturing, and integrated manufacturing (e.g., load-bearing mechanical structures and components embedded with electronic, optical, magnetic, or biological components). Indeed, in some cases it may be the only viable and practical method for determining local and volume-averaged properties, as, for example, in the context of evaluating in situ thin-film mechanical properties or mapping the local mechanical property variations across grain/phase boundaries or along gradients in structures (8). Similarly, in order to evaluate detailed layer-by-layer mechanical characteristics of a three-dimensionally (3D) printed material, instrumented indentation appears to be the only practically viable method to probe how processing conditions lead to evolution of properties and structural integrity. With the commercial availability of sophisticated and inexpensive

Significance

Instrumented indentation has emerged as a versatile and practical means of extracting material properties, especially when it is difficult to obtain traditional stress–strain data from large tensile or bend coupon specimens. Accurately solving the inverse problem of depth-sensing indentation is critical for the determination of the elastoplastic properties of materials for a wide variety of structural and functional applications in engineering components. Utilizing the latest developments in deep learning that invoke neural networks and multifidelity datasets, we have developed a general framework for extracting elastoplastic properties of engineering alloys with markedly improved accuracy and training efficiency than has been possible thus far. We validate this method by assessing estimates of extracted properties in direct comparison with independent experimental measurement.

Author contributions: L.L., M.D., U.R., G.E.K., and S.S. designed research; L.L., M.D., and P.K. performed research; L.L., M.D., P.K., U.R., G.E.K., and S.S. analyzed data; L.L., M.D., and G.E.K. developed the multifidelity deep-learning algorithms; G.E.K. and S.S. supervised the project; and L.L., M.D., P.K., U.R., G.E.K., and S.S. wrote the paper.

Reviewers: J.L., IMDEA Materials Institute; and T.Z., Georgia Institute of Technology.

Competing interest statement: L.L., M.D., G.E.K., and S.S. have filed a patent application based on the research presented in this paper.

Data deposition: The code and related input data have been deposited in GitHub at https://github.com/lululxvi/deep-learning-for-indentation.

[1]L.L. and M.D. contributed equally to this work.

[2]To whom correspondence may be addressed. Email: mingdao@mit.edu, george_karniadakis@brown.edu, or ssuresh@ntu.edu.sg.

This article contains supporting information online at https://www.pnas.org/lookup/suppl/doi:10.1073/pnas.1922210117/-/DCSupplemental.

First published March 16, 2020.

robotic tools, depth-sensing indentation measurements can readily be incorporated into the processing and fabrication of materials and components by such means as layer-by-layer additive manufacturing.

In general, a forward indentation algorithm for a metallic material provides indentation response (i.e., force vs. displacement [P vs. h] curve during indentation loading and retraction of the indenter) for a given set of elastoplastic properties (elastic modulus, Poisson's ratio, yield strength, strain-hardening exponent, and tensile strength). The inverse indentation problem, on the other hand, should lead to the unique determination of the elastoplastic properties from a set of indentation P–h data.

The hardness (H) of a material has long been used as a property from which yield strength (σ_y) can be estimated (7, 8, 15, 16), although their connection is known to be only highly approximate (5, 16). In order to address this limitation of simple hardness measures, dimensional analyses and scaling functions have been developed (5, 8, 17), and explicit universal scaling functions have been established for solving the forward and inverse problems in depth-sensing indentation by recourse to single (5) and multiple sharp indenter tip geometries (6, 18–20). Additionally, studies have also focused on efforts to extract elastoplastic properties from load–displacement curves for spherical indenters (21–25). Due to the inherent difficulties in accurately accounting for the contact area and the initial contact point involved with spherical indentation, and given that spherical indentation introduces an additional dimension (i.e., the indenter diameter), which needs to be properly reconciled with the various structural dimensions of the material being tested, sharp indentation has become the more preferred method. We therefore focus our present study on sharp indentation, with the full recognition that the tip radius effects of nominally "sharp" indenters need to be carefully accounted for in relation to the depth of penetration of the indenter into the material and the characteristic structural dimensions of the material, so as to avoid the effects of the radius of the sharp indenter tip on the estimated properties of the materials.

The high sensitivity of traditional brute force calculations to solve the inverse indentation problem and the uncertainty inherent in such calculations in uniquely extracting elastoplastic properties from indentation responses are known to arise from functional nonlinearity (5, 6, 9). Furthermore, there are presently no general methods available that can accurately account for tip radius effects on the elastoplastic properties extracted from indentation analyses. This situation is further compounded by the fact that within a portion of the parametric space for the wide spectrum of engineering materials for which instrumented indentation could serve as a useful property assessment tool, the inverse indentation problem may not provide a unique set of predictions for mechanical properties from the indentation data. Therefore, there exists a critical need to explore new ways of determining the elastoplastic properties of materials from depth-sensing instrumented indentation with a greater degree of confidence in their uniqueness, accuracy, and fidelity before the potential for the broad adoption of the method for many emerging areas of technology can be fully realized. Furthermore, to establish a scalable method for a wide variety of applications, and to minimize errors in extracting mechanical properties, it becomes inevitable to assess ways in which the latest developments in deep learning (DL) can be employed to harvest significant improvements for solving the inverse indentation problem.

Recent Advances in DL and Multifidelity Methods

Recent developments of data-driven methods, such as deep neural networks (NNs), provide us with opportunities that cannot be tackled solely through traditional methods. In addition to well-known applications of machine-learning (ML) algorithms in such fields as image/video analysis (26, 27) and natural language processing (28), ML has also been used for various engineering problems, such as in the discovery of new materials (29) and in health care (30). However, data-driven methods usually require a large amount of data to train the NN model, and in many engineering problems, it is often difficult to obtain necessary data of high accuracy. In these situations, it may be advantageous to complement the dataset of expensive experimental measurements by employing synthetic data derived from simulations of physical models. An example of such an approach entails the use of density functional theory calculations to train NNs so that DL algorithms can be developed to determine the least energetically expensive means of modulating the bandgap of a semiconductor material through elastic strain engineering (31).

Multifidelity methods (32) using Bayesian modeling to integrate high- and low-resolution simulations can serve as one possible means for training data. This type of data fusion could help to train DL models when limited experimental data that lead only to insufficient levels of accuracy are available. The training data could come from different sources, e.g., from instruments with different resolutions and/or from simulations using different levels of accuracy in predictive capabilities. The multifidelity method (32) is hierarchical so that high-fidelity and low-fidelity data can be identified and assigned to train DL algorithms. This Bayesian multifidelity modeling based on Gaussian process regression (GPR) (33) can also alleviate the extreme computational cost of training. However, the GPR method suffers from two critical shortcomings: 1) it is computationally prohibitive to manage big datasets, and 2) it is not sufficiently accurate when dealing with nonlinear correlations. To overcome some of these limitations, it is possible to resort to a scalable multifidelity approach based on NNs (34), although the efficacy of such an approach has not yet been tested and validated for applications. In this work, we present a multifidelity NN (MFNN) method that is capable of fusing together different sets of data with different fidelity levels, arising from different experimental measurement accuracy or from different levels of sophistication of computational modeling (e.g., two-dimensional [2D] vs. 3D computational simulation and different levels of finite element mesh refinement).

Prior Work on ML for Computational Mechanics and Inverse Indentation Problems

Some prior work has explored use of ML to solve both forward and inverse problems in computational mechanics and, in particular, has trained NNs to extract material properties from instrumented indentation data. The training process in these cases usually involved fitting a numerical simulation dataset. For example, based on data points of spherical indentation load–displacement curves from finite-element simulations, a trained NN was established to estimate material parameters (35–38). Trained NNs were generated to reproduce the loading portion of sharp nanoindentation load–displacement curves (39). A NN-based surrogate model was used in order to reduce the number of finite-element method (FEM) conical indentation simulations to extract material properties (40). Besides NNs, other ML approaches have also been employed to solve the indentation problems, such as identification of plastic properties from conical indentation using Bayesian-type analysis (41). These methods, however, were generally cumbersome to use in practice as they required training using all data points within individual indentation loading (and/or unloading) curves or extensive iterations with finite-element simulations. In addition, they were not systematically tested throughout the broad parameter space for a wide variety of engineering materials to establish their predictive capabilities and levels of accuracy. They have also not been extensively validated by comparisons with experimental observations. In summary, the latest advances in DL have not yet been fully utilized for solving a highly nonlinear inverse problem, such as that involving an inverse indentation problem.

Objectives of the Present Study

In the present study, we present a unique combination of the latest developments in DL and multifidelity methods with the specific objective of significantly enhancing the accuracy, reliability, and predictability of mechanical properties of elastoplastic materials from inverse analyses of depth-sensing instrumented indentation results. Specifically, this study is aimed at achieving the following objectives:

1) Establish algorithms for solving the inverse problem in instrumented indentation for single, dual, and multiple indentation, whereby the elastoplastic properties of the indented material can be predicted with much greater accuracy than currently feasible through traditional brute force computation and function-fitting methods that rely on the same set of available training data.
2) Establish a scalable and stable MFNN that can
   a) significantly reduce the required number of high-fidelity data for instrumented indentation to achieve a desired level of accuracy in the prediction of mechanical properties;
   b) utilize known physical and scaling laws to improve training efficiency and prediction accuracy; and
   c) integrate simulation data and experimental data for training in order to significantly reduce systematic errors, in indentation analyses, arising from material variability or experimental conditions.
3) Validate the methods presented here through direct comparisons with indentation experiments for several different materials, including two traditionally made (wrought) 6061 and 7075 aluminum alloys and six 3D printed Ti-6Al-4V alloys.

Results

We begin here with a graphical illustration of problem statement in Fig. 1, showing the forward and reverse analysis of sharp instrumented indentation (Fig. 1*A*), in order to connect our results to the relevant parameters and nomenclature. Representations of the NN architecture are shown for the single-fidelity (Fig. 1*B*) datasets, the multifidelity datasets (Fig. 1*C*) without residual connection (34), and the multifidelity datasets proposed in this work with residual connection (Fig. 1*D*). In this section, we first show the results using the single-fidelity NN architecture (Fig. 1*B*) to demonstrate how they improve the estimation of mechanical properties of elastoplastic materials compared to those extracted solely from previously established dimensionless fitting functions for inverse analysis of conical indentation (5). These fitting functions were obtained based on brute force finite-element simulations covering the commonly observed elastic and power-law plastic parameter space for engineering metals (5) and using the dimensional analysis of indentation process (3, 5, 17). This is followed by training the NNs on results from 2D and 3D simulations of conical or Berkovich indentation tests using the FEM. Subsequently, we extend the scope of the DL analyses to include results from different multifidelity approaches. For all of these results, we compare them with experimental results involving using the Berkovich indentation on Al-6061, Al-7075, and 3D printed Ti alloys. More details of the method and nomenclature used in the present study can be found in *Methods* and *SI Appendix*.

Improving Inverse Analysis Results for Sharp Indentation Using Single-Fidelity NN Architecture.

Training NNs using data generated from dimensionless fitting functions. To demonstrate that NNs are capable of representing the correlation between (C, dP/dh, W_p/W_t) and E^* (or σ_y), where C, dP/dh, and W_p/W_t are loading curvature, initial unloading slope, and the ratio of residual plastic work and total work, respectively (see more details in *SI Appendix*), we first generate a dataset using the previously established dimensionless fitting functions. The data points used for fitting were obtained through FEM simulations covering commonly observed elastic and power-law plastic parameter space for engineering metals in ref. 5 for conical indentation with a half included-tip-angle of 70.3°. We then train NNs using these data points (*SI Appendix*, Fig. S1*A*). The mean absolute percentage error (MAPE) defined as follows,

$$\mathrm{MAPE} = \frac{1}{N}\sum_{i=1}^{N}\left|\frac{A_i - F_i}{A_i}\right|,$$

is calculated against the same dataset, where N is the number of data points, and A_i and F_i are the true and prediction values of

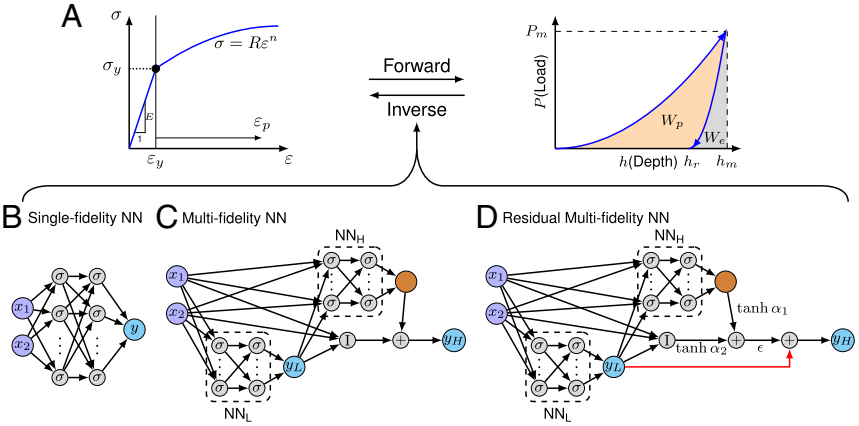

Fig. 1. DL methods to solve inverse problems in depth-sensing instrumented sharp indentation. (*A*) Schematic illustration of the power-law elastoplastic stress–strain behavior used in the present study (*Left*) and a typical load (P) vs. displacement (h) response of an elastoplastic material to instrumented sharp indentation (*Right*). (*B–D*) Flowcharts of the NNs for solving (*B*) single-fidelity inverse problems, e.g., single indentation, and dual/multiple indentation, and (*C* and *D*) multifidelity inverse problems involving datasets of different fidelity and accuracy. Input variables such as x_1 and x_2 represent parameters such as C, dP/dh, and W_p/W_t, and output variable y represents material properties such as E^* or σ_y. We only show two variables as the NN inputs for clarity, but the number of inputs could be three or four for single indentation or dual/multiple indentation problems. The NN inputs of all cases and training datasets used are summarized in *SI Appendix*, Tables S1 and S2. (*C*) The original MFNN in ref. 34. (*D*) The MFNN proposed in this paper involves a residual connection (red line) from the low-fidelity output y_L to the high-fidelity output y_H. σ and I are the nonlinear and linear activation functions, respectively.

the ith data point, respectively. We observe from *SI Appendix*, Fig. S1*A* that the errors associated with the extracted values of yield strength σ_y (~50% or higher) are much larger than those for the effective indentation elastic modulus, E^* (~10%). This is an illustration of the inherently high sensitivity of the inverse problem, especially for plastic properties. As expected, when only data generated from the fitting functions for training are used, the trained NNs do not perform any better than the fitting functions, and only reach the same performance with a high number of training data points.

Training NNs using data obtained from 2D FEM simulations. Next, we consider a dataset generated by conical (2D axisymmetric) FEM simulations (see ref. 5 for model setup). The FEM dataset involved simulations for 100 different elastoplastic parameter combinations, and we removed three data points with $n > 0.3$ and $\sigma_y/E^* \geq 0.03$, where the inverse problem may have nonunique solutions. The possible nonuniqueness comes from the fact that increasing elastic modulus, plastic yield strength, or strain-hardening exponent can all result in an increased loading curvature, with the consequence there may exist multiple elastoplastic parameter sets in achieving nearly identical indentation loading/unloading curves (see more detailed discussions in ref. 5). The green curves with solid square symbols in Fig. 2 *A* and *B* (also see *SI Appendix*, Fig. S1*B*) show the results of training NNs for E^* and σ_y using different numbers of conical indentation FEM simulation data points. By using merely 20 training points for E^*, the trained NN already performs better than the previously established fitting functions in ref. 5. For σ_y, 50 or more data points are required to achieve better accuracy than the previous algorithm established by direct fitting of the finite-element data points (5). With 80 data points for training, the average error for E^* can be improved to ~5% significantly lower than ~8% from using the algorithm established in ref. 5.

Training NNs using FEM data obtained from multiple indenter geometries. Fig. 2 shows the results of training NNs for E^* and σ_y using two or four indenters with different tip geometries. The trained two-indenter and four-indenter NNs perform better than the single-indention NNs. More indenter geometries improve accuracy. With a large enough size of training datasets (≥20 for E^*; ≥90 for σ_y with two indenters; and ≥60 for σ_y with four indenters), the trained NNs begin to outperform the dual-indentation algorithm (6). For the trained two-indenter NNs, the average error for E^* is about 2%—much better than that achieved in ref. 5 or 6 using traditional fitting functions. For the trained four-indenter NNs, the average error for E^* is <2%, and for σ_y, the average error becomes <7%. Note that with traditional algorithms, it is not straightforward to utilize "redundant" information for solving unknown variables, while in the case of training the two-indenter or four-indenter NNs more/redundant input variables and data can be easily utilized to improve accuracy in the estimation of elastic and plastic properties.

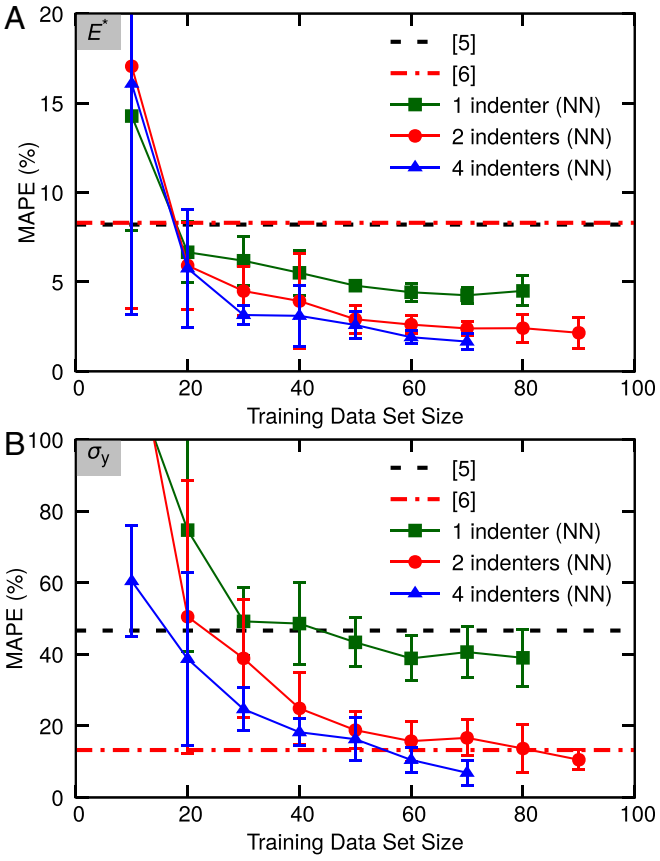

Fig. 2. Results of mean absolute percentage error (MAPE) as a function of the training dataset size for single, dual, and multiple indenters. Results of training NNs for (*A*) E^* and (*B*) σ_y using computational simulations of sharp conical indentation using FEM with one, two, or four different indenter tip geometries. The black dotted line and the red dash-dotted line show the average error of directly applying the single-indentation fitting functions in ref. 5 and dual-indentation fitting functions in ref. 6, respectively. The one-indenter data are obtained using conical tip with 70.3° half-included tip angle; the two-indenter data are obtained using conical tips with 70.3° and 60° half-included tip angles; and the four-indenter data are obtained using conical tips with 70.3°, 50°, 60°, and 80° half-included tip angles.

Inverse Analysis Using MFNNs.

Approach 1: Integrating data generated from fitting functions (low fidelity) and FEM simulation data (high fidelity). In this example, we test the multifidelity approach for the conical single-indentation data using only materials with $n \leq 0.3$ (which still covers the material parameter space for a wide spectrum of engineering metals and alloys), as shown in Fig. 3 *A* and *B*. The low-fidelity data use 10,000 (for E^*) or 100,000 (for σ_y) data points from the formulas in ref. 5, and the high-fidelity data are from the finite-element simulations. All data in Fig. 3 *A* and *B* pertain to a conical (2D axisymmetric) indenter with a half-included tip angle of 70.3°. By using the multifidelity approach, 1) higher accuracy is achieved compared to using only high-fidelity data, and 2) the number of high-fidelity data points required for achieving high accuracy is also significantly reduced. Only 10 high-fidelity data points are needed to achieve 5% average error for E^*, and only 40 high-fidelity data needed to achieve better accuracy for σ_y than the traditional fitting functions (5).

Here, we compare our MFNN method using the residual connection technique introduced in this paper (Fig. 1*C*; see more details in *Methods*) with the MFNN used in ref. 34 without the residual connection (Fig. 1*B*). We test the performance of these two methods on the property predictions based on multifidelity datasets as described in *Methods*. Note that in this case low fidelity refers to data obtained using the fitting functions, and high fidelity refers to 2D FEM data. *SI Appendix*, Fig. S2*A* (blue line) shows that the training of the original MFNN is quite unstable with a large standard deviation. When comparing the mean error of E^* in *SI Appendix*, Fig. S2*A* (blue and red lines), note that the error becomes more stable, i.e., the training of NNs becomes more stable with the addition of residual connection. For those well-trained networks, the error in E^* is similar. Furthermore, as shown in *SI Appendix*, Fig. S2*B*, our proposed MFNN with the residual connection also achieves higher accuracy than the fitting functions for the case of σ_y, in addition to being more stable.

Approach 2: Integrating 2D axisymmetric FEM data (low fidelity) and 3D FEM data (high fidelity). Fig. 3 *C* and *D* show the results of MFNNs trained by integrating 2D axisymmetric FEM simulation results

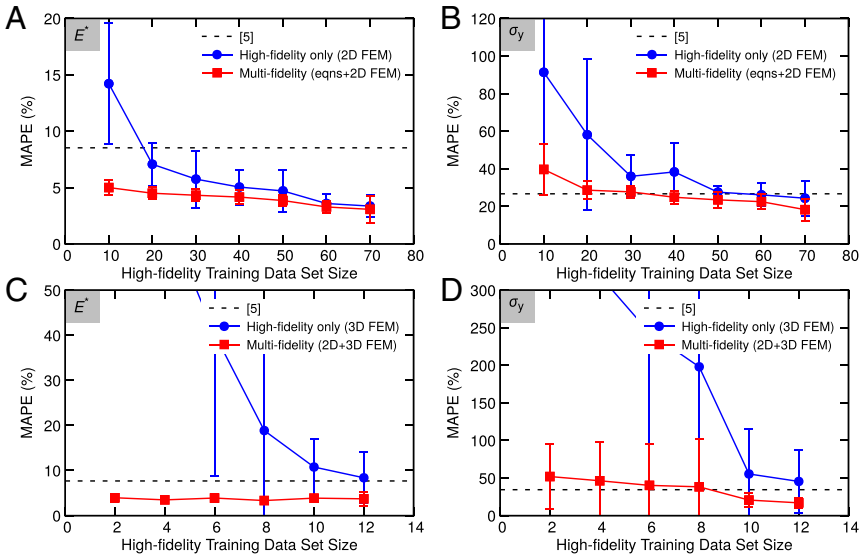

Fig. 3. Mean average percentage error as a function of training dataset size for MFNNs trained by 2D and 3D FEM simulations of inverse indentation. (*A* and *B*) Results of MFNNs trained by integrating low-cost low-fidelity data using fitting functions (5) together with limited number of high-fidelity FEM data for (*A*) E^* and (*B*) σ_y. In *A* and *B*, the low-fidelity data use 10,000 (for E^*) or 100,000 (for σ_y) data points from the formulas in ref. 5. All 2D axisymmetric FEM data are assuming a conical indenter with a half-included tip angle of 70.3°. (*C* and *D*) Results of MFNNs trained by integrating 2D axisymmetric FEM results (low fidelity) together with 3D FEM simulation data (high fidelity) for (*C*) E^* and (*D*) σ_y. The low-fidelity 2D FEM data in *C* and *D* include 97 axisymmetric FEM simulations with different elastoplastic parameters. All 3D FEM data are using a 3D Berkovich indenter, which has a three-sided pyramid sharp tip that can maintain its self-similar geometry to very small indentation depth. The Berkovich indenter has a half-angle of 65.3°, measured from the tip axis to one of the pyramid surfaces.

(low fidelity) together with 3D FEM simulation data for a Berkovich indenter (high fidelity) to estimate E^* and σ_y. Here, MAPE is calculated with respect to the 3D FEM data, which have higher fidelity than the 2D axisymmetric FEM data. Although conical indentation FEM results with a 70.3° included half-angle are considered good approximations of the actual indentation results from a 3D Berkovich or Vickers indenter tip (5, 6, 9, 18–20), significant errors can still occur due to the inherent high sensitivity of the inverse problem, especially for extracting plastic properties, as shown in Fig. 3 *C* and *D*. The foregoing results illustrate that the multifidelity approach leads to much more accurate estimates of mechanical properties from instrumented sharp indentation data with a smaller number of high-fidelity data points than both the single-fidelity approach and the fitting functions.

Approach 3: Integrating high-fidelity experimental data and synthetic data for error correction. Here, we first test the trained NNs obtained above (approach 2) for the Berkovich indenter tip for two indentation experimental datasets from traditional (wrought) Al alloys Al6061-T6511 (six experiments) and Al7075-T651 (six experiments) with the indentation characteristics summarized in *SI Appendix*, Table S3. The indentation raw datasets used are the same as those used in ref. 5, and $\frac{dP}{dh}\big|_{h_m}$ is evaluated by the best linear fitting within 5% of each unloading curve. The elastoplastic properties of Al6061-T6511 are Young's modulus $E = 66.8$ GPa ($E^* = 70.2$ GPa), yield strength $\sigma_y = 284$ MPa, and strain-hardening exponent $n = 0.08$; and the properties of Al7075-T651 are $E = 70.1$ GPa ($E^* = 73.4$ GPa), $\sigma_y = 500$ MPa, and $n = 0.122$. In addition, to reduce the incurred systematic experimental errors, we use NNs to learn from three randomly selected experimental data points added as high-fidelity data in the NN training process in multifidelity approach 3. Specifically, the low-cost 2D axisymmetric finite-element datasets are still used as low-fidelity data, and the limited number of 3D Berkovich indentation finite-element data are used together with three additional experimental data points as high-fidelity data for the case of Al6061-T6511 or Al7075-T651 alloy. There are up to 20 unique combinations for randomly selecting three out of six experiments in each case. Here, the results are obtained by exhausting all 20 possibilities.

Fig. 4*A* summarizes the inverse analysis results using different approaches. The NNs trained by 2D axisymmetric FEM results (low fidelity) together with 3D FEM simulation data (high fidelity) perform better than the previous established equations in ref. 5. The NNs trained by adding experimental results as high-fidelity training data to the 2D and 3D FEM data perform very well for both E^* and σ_y with MAPE less than 4% for both Al6061-T6511 and Al7075-T651, leading to significantly improved accuracy for σ_y with this "hybrid" multifidelity approach. Assuming power-law strain-hardening behavior, our proposed method can also be used to extract strain-hardening characteristics from instrumented indentation. To achieve that, we first train NNs to predict stresses at different plastic strains, and then compute the strain-hardening exponent by least-squares fitting of the power-law hardening function.

Fig. 4*B* shows the inverse analysis results of using MFNNs to extract additional data points from the stress–strain curve (i.e., to determine strain-hardening behavior), where selected stress values at 3.3%, 6.6%, and 10% plastic strains are obtained. The NNs trained by adding experimental results as part of the high-fidelity training data also perform very well for $\sigma_{3.3\%}$, $\sigma_{6.6\%}$, and $\sigma_{10\%}$ with MAPE less than 4% for both Al6061-T6511 and Al7075-T651, significantly improving the accuracy for evaluating stresses at different plastic strain using the hybrid multifidelity approach. Fig. 5 shows the corresponding stress–strain curves obtained by least-square fitting of the power-law hardening behavior, exhibiting good matching of the experimental data (with experimentally extracted hardening exponent $n = 0.08$ and 0.122), whereas $n = 0.073$ and 0.127 for Al6061-T6511 and Al7075-T651, respectively, estimated using the hybrid multifidelity approach. Note that when hardening is low (i.e., $n \to 0$), directly estimated errors of n can be misleading because very small variations in hardening response can lead to large fractional errors for elastic-perfectly plastic metal alloys. Comparing errors in stresses at different plastic stains is a

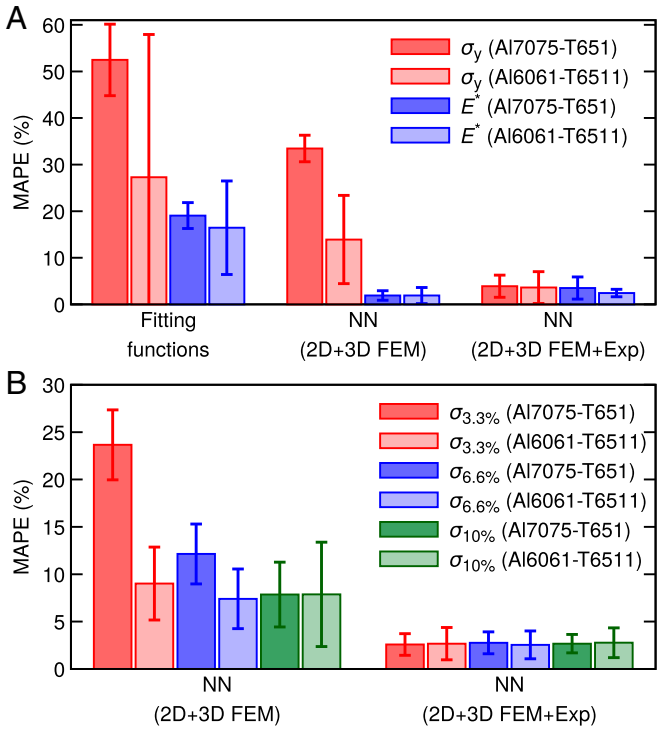

Fig. 4. Inverse analysis results of mean average percentage error (MAPE) of (*A*) E^* and σ_y, and (*B*) $\sigma_{3.3\%}$, $\sigma_{6.6\%}$, and $\sigma_{10\%}$ for two aluminum alloys Al6061-T6511 and Al7075-T651 (here, the subscripts 3.3%, 6.6%, and 10% for σ represent plastic strains). The results labeled as "fitting functions" are obtained directly using previously established equations in ref. 5. The results labeled as "NN (2D + 3D FEM)" are obtained using NNs trained by integrating 2D axisymmetric FEM data (low fidelity) with 3D Berkovich FEM data (high fidelity), and the results labeled "NN (2D + 3D FEM + EXP)" are obtained using NNs trained by adding experimental results as high-fidelity training data in addition to the 2D and 3D FEM training data.

more objective way in evaluating the accuracy with respect to the stress–strain behavior or the hardening behavior.

Next, we test the NN algorithms on an extensive set of experiments performed on six different, 3D printed, Ti-6Al-4V alloys. Full details of the 3D-printing conditions, the ensuing microstructures of the six Ti alloys, and the tensile stress–strain characteristics are all available in ref. 42. The six 3D printed Ti alloys with different microstructures are designated as B3067, B3090, B6067, B6090, S3067, and S6067 (42). We carried out depth-sensing instrumented nanoindentation experiments of these 3D printed Ti alloys using the method described in *Methods*. There are 144 repeated indentations conducted for each 3D printed Ti alloy. We perform inverse analyses of these six alloys and estimate their elastoplastic properties using the various ML approaches introduced in this paper. We then compare these predictions with direct and independent experimental assessments of the elastoplastic properties of the six alloys from the tensile stress–strain responses obtained in ref. 42. *SI Appendix*, Table S4*A* summarizes the indentation characteristics of six 3D printed Ti-6Al-4V alloys extracted directly from raw indentation curves. *SI Appendix*, Table S4*B* lists the indentation characteristics of two 3D printed titanium alloys from indentation curves corrected with an estimated indenter tip radius of 0.6 μm (see details of the tip radius estimation and tip radius effect correction method in *SI Appendix*, based on the method suggested in ref. 43), all using the same experimental setup with a maximum indentation load of 9 mN for each indentation experiment. The yield strength values, σ_y, of B3067, B3090, B6067, B6090, S3067, and S6067 are 1,121, 1,168, 1,102, 1,151, 1,121, and 1,063 MPa, respectively, and the nominal Young's modulus of these 3D printed Ti alloys is E = 110 GPa (E^* = 109.6 GPa).

For indentations made on Ti-6Al-4V (B3067), Fig. 6 summarizes the inverse analysis results using the different approaches introduced in this paper for both E^* and σ_y. The results labeled as "NN (raw)" and "NN (tip)" are obtained by applying NNs trained by integrating 2D axisymmetric FEM data (low fidelity) with 3D Berkovich FEM data (high fidelity), either by directly applying the raw indentation data or by using the indentation data after correcting the raw data for the indenter tip radius effects, respectively. NNs trained using only FEM data, when operating directly on raw indentation data, exhibit medium accuracy of 24.2 ± 4.6% MAPE in estimating the elastic modulus, but an unacceptably high MAPE of 105.5 ± 16.7% in evaluating σ_y. However, when tip radius effect-corrected indentation data are used in the analyses, we observe significantly reduced inverse analyses errors for both E^* (MAPE = 5.4 ± 3.1%) and σ_y (MAPE = 40.3 ± 8.3%). With tip radius effect correction, we find that the extracted values of E^* and σ_y are much closer to the uniaxial test results shown in figure S1 in ref. 42. When using the NN (raw) results, it is evident that systematic bias occurs in the extraction of both E^* and σ_y; from the NN (tip) results, there appears to be systematic bias for σ_y, even after the significant improvement in predictive capability by applying tip radius effect correction.

We now apply our multifidelity approach 3 described in *Methods* in an attempt to further reduce systematic errors in the inverse analyses. For this purpose, we randomly select five experimental data points out of 144 as additional input to high-fidelity data in the NN training process. Specifically, the low-cost 2D

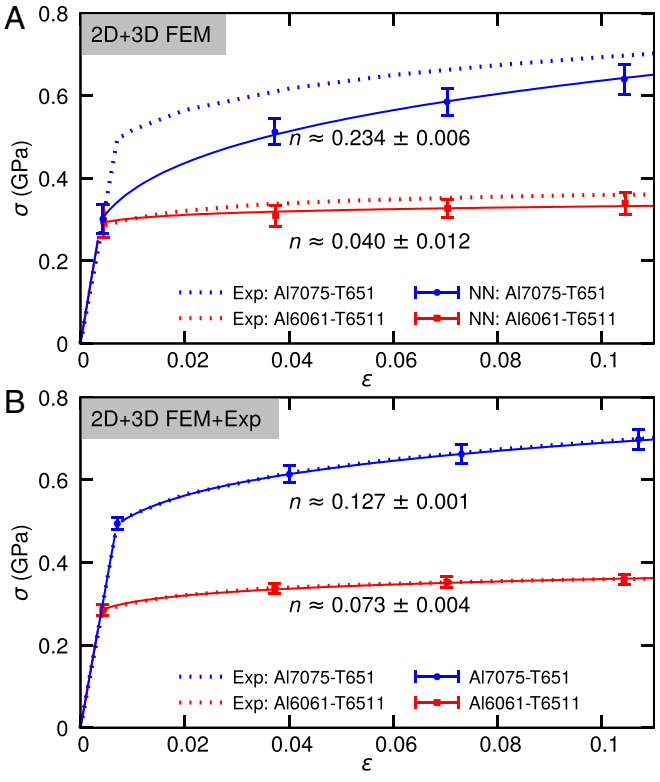

Fig. 5. Inverse analysis results of hardening exponent for two aluminum alloys Al6061-T6511 and Al7075-T651. The hardening exponent is obtained by least-squares fitting of σ_y, $\sigma_{3.3\%}$, $\sigma_{6.6\%}$, and $\sigma_{10\%}$ predicted by NNs trained by (*A*) 2D and 3D FEM data, and (*B*) 2D, 3D FEM data and three experimental data points. Here, the subscripts 3.3%, 6.6%, and 10% for σ represent plastic strains.

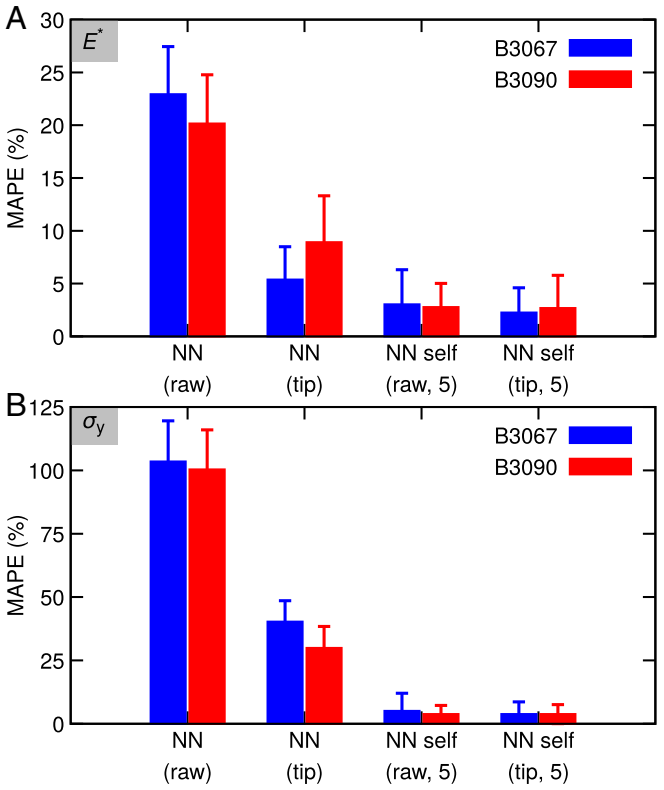

Fig. 6. Inverse analysis results of (*A*) E^* and (*B*) σ_y for two 3D printed Ti-6Al-4V alloys B3067 and B3090. The results labeled "NN (raw)" and "NN (tip)" are obtained by applying NNs trained by integrating 2D axisymmetric FEM data (low fidelity) with 3D Berkovich FEM data (high fidelity), using directly the raw indentation *P*–*h* data and using the tip radius effect-corrected indentation data, respectively. The results labeled "NN self (raw, 5)" and "NN self (tip, 5)" are obtained by applying NNs trained by adding five randomly picked experimental indentation curves as high-fidelity training data in addition to the 2D and 3D FEM training data, using directly the raw indentation data and using the tip radius effect-corrected indentation data, respectively. Full details of the experimental data on instrumented indentation and stress–strain response for both B3067 and B3090, along with the conditions for 3D printing and depth-sensing indentation, and microstructure evolution can be found in ref. 42; a brief summary of these literature data are provided in *SI Appendix*.

axisymmetric finite-element datasets are still used as low-fidelity data, while the limited number of 3D Berkovich indentation finite-element data are used together with three additional experimental data points as high-fidelity data. The results are pooled together by exploring the full spectrum involving 10 uniquely different ways of random selection of such data. In Fig. 6, the results labeled "NN self (raw, 5)" and "NN self (tip, 5)" are obtained by applying NNs (trained by adding the five randomly selected B3067 experimental indentation curves as high-fidelity training data in addition to the 2D and 3D FEM training data) to the raw indentation data and to the tip radius effect-corrected indentation data, respectively. NNs, trained using the hybrid multifidelity approach that included the added experimental training data now significantly reduce errors when operating directly on raw indentation data and when operating on tip radius effect-corrected indentation data. Specifically, for E^* MAPE drops to 3.0 ± 3.3% and 2.3 ± 2.4% for raw indentation data and tip radius-corrected data, respectively, and for σ_y MAPE drops to 5.1 ± 7.0% and 3.9 ± 4.8%, respectively. Although NNs operating on tip radius effect-corrected data still perform better, the hybrid multifidelity approach introduced here is found to be substantially more effective in learning from the data and in correcting errors from tip radius effects and other systematic biases arising from uncorrected raw data. Similar results are shown for indentations made on another 3D printed Ti-6Al-4V alloy (B3090) in Fig. 6 for both E^* and σ_y.

Finally, we test a more practically useful variation of hybrid multifidelity approach. Here, we aim to reduce systematic errors by randomly selecting indentation experimental data points from a different calibration material (while using the same experimental/postprocessing setup) as added high-fidelity data in the NN training process in multifidelity approach 3. Specifically, the low-cost 2D axisymmetric finite-element datasets are still used as low-fidelity data while the limited number of 3D Berkovich indentation finite-element data are used together with some additional experimental data points from a different calibration material B3067 (with 1 to 20 data points randomly selected from a total of 144 data points) as high-fidelity training data; the trained NNs are used to analyze B3090 indentation data.

Fig. 7 summarizes the indentation inverse analysis results for B3090 using this approach (denoted as "Peer") compared to the results where the added high-fidelity training data are from the same material (B3090) with the same experimental conditions (denoted as "Self"). Here, MAPE (log scale) is plotted against the number of randomly selected experimental training data, n_{exp} (linear scale) from either the same material (Self) or from another Ti alloy (Peer). Except when no experimental data are added for training (at 0), each data point in Fig. 7 represents the results pooled together from 10 uniquely different ways of random selection. The notion of "(raw)" and "(tip)" in the labels

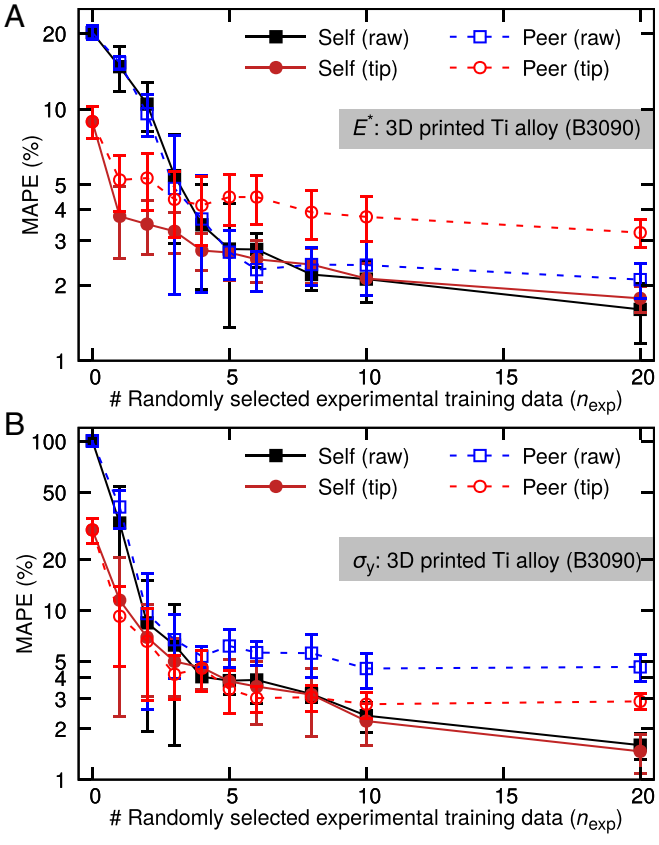

Fig. 7. Inverse analysis of a 3D printed Ti-6Al-4V alloy B3090. (*A*) E^* and (*B*) σ_y vs. the number of randomly selected experimental training data either from B3090 (denoted as Self) or from B3067 indentation experiments (Peer). The notion of "(raw)" and "(tip)" in the labels indicate all experimental data used are from the uncorrected raw indentation data and the tip radius effect-corrected indentation data, respectively.

indicate all experimental data used are either the uncorrected raw indentation data or those corrected for tip radius effects, respectively. It is clear from Fig. 7 that adding experimental training data from the same material (Self) or from a different calibration material (Peer) under the same experimental conditions can significantly reduce systematic errors for both E^* (MAPE < 4%) and σ_y (MAPE < 5%). However, we note that the benefits of adding experimental training data begins to saturate when $n_{exp} \geq 5$. With sufficient training data, the hybrid multifidelity approach shows remarkable ability to learn and correct from the raw data any systematic errors from tip radius effects and other factors directly. As expected, adding experimental training data from the same material (Self cases) normally performs better than adding from a different calibration material (Peer cases) under the same experimental conditions; in particular, we observe error reduction at $n_{exp} = 20$ by as much as one and two orders of magnitude for estimating E^* and σ_y, respectively, from the inverse analysis.

Fig. 8 and *SI Appendix*, Fig. S4 summarize the inverse analysis results of MAPE for E^* and σ_y for 3D printed Ti-6Al-4V alloys (B3067, B3090, B6067, B6090, S3067, and S6067) as a function of n_{exp} for randomly selected experimental training data from B3067 indentation experiments. Except when no experimental data are added for training (at 0), each data point represents the results pooled together from 10 uniquely different ways of such random selection. All indentation experimental data used are from the uncorrected raw indentation data. The black dashed line is the Self training case for B3067, while the curves representing other colors are the Peer training cases using B3067 indentation data for training. Again, all of the trends noted in Fig. 7 are also observed here in Fig. 8 and *SI Appendix*, Fig. S4, showing the general applicability of this hybrid multifidelity approach by adding Peer experimental data as high-fidelity training data for improved inverse analysis accuracy.

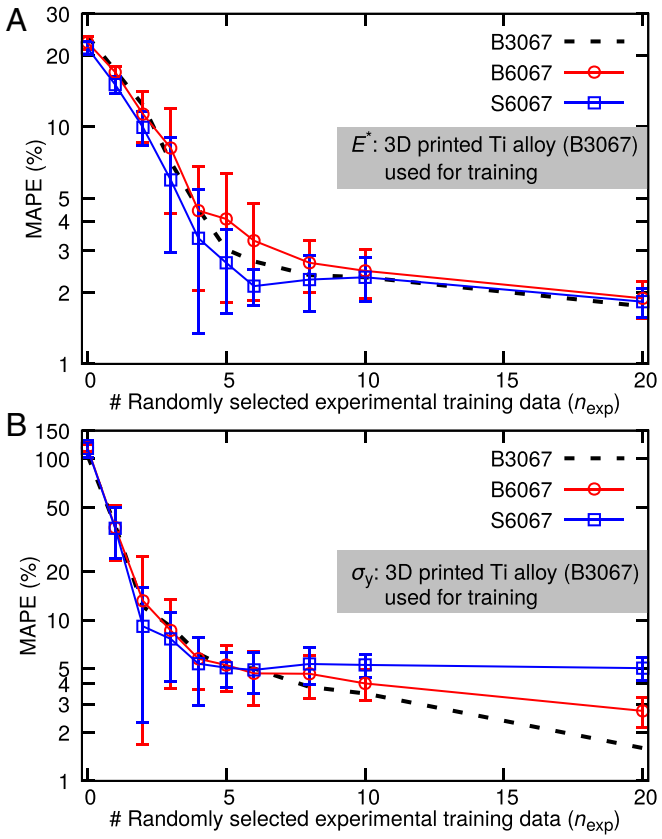

Fig. 8. Inverse analysis of three 3D printed Ti-6Al-4V alloys. (*A*) E^* and (*B*) σ_y for 3D printed Ti-6Al-4V alloys (B3067, B6067, and S6067) vs. the number of randomly selected experimental training data from B3067 indentation experiments. All experimental data used are from the uncorrected raw indentation data. See also *SI Appendix*, Fig. S4 for additional comparisons.

Assuming, once again, power-law strain-hardening behavior, we can evaluate stresses at different plastic strain values, and then compute the strain-hardening exponent by least-squares fitting of the power-law hardening function for 3D printed titanium alloys. Fig. 9 shows the inverse analysis results of selected stresses at 0% (i.e., σ_y), 0.8%, 1.5%, and 3.3% plastic strains and the fitted stress–strain curves for two 3D printed Ti-6Al-4V alloys using the hybrid multifidelity approach. Analogous to evaluating the yield strength (stress at zero plastic strain), our predicted stress–strain curves are close to the experimental curves when a few experimental data points are added as part of the high-fidelity data for the training of NNs.

Transfer Learning. In the results presented so far, the hybrid training of NNs for each aluminum alloy and each 3D printed titanium alloy is conducted with a fresh start without any direct connections to the other trained NNs. On the other hand, to speed up the training of NNs, we have also developed a transfer learning technique, where the whole multifidelity network (both low- and high-fidelity subnetworks) is first trained using all of the 2D and 3D FEM data as baseline training. Next, given the additional new experimental data, only the high-fidelity subnetwork is further trained using these additional experimental data points. The errors from the networks before and after transfer learning are shown in Fig. 10. This figure indicates that we can first establish a comprehensive baseline training and then add additional case-specific training later for improved training efficiency and faster accumulated learning.

Discussion and Concluding Remarks

We have demonstrated in this work a general framework for extracting elastic and plastic properties of engineering alloys through a suite of unique approaches that combine the latest advances in depth-sensing instrumented indentation with computational simulations of the mechanical properties of materials and the latest developments in DL using NNs. We have shown how different single-fidelity and multifidelity approaches can be customized to extract different levels of accuracy, even when only a small set of training data are available. Furthermore, our method establishes how long-recognized and hitherto-unaddressed limitations of extracting plastic properties of materials from indentation data, such as uniqueness of the estimated property values, systematic errors, and uncertainties arising from the effects of tip radius of nominally sharp indenters, can be overcome to produce a significantly higher level of accuracy and fidelity in the inverse analysis approach.

We have introduced in this work three multifidelity approaches, along with single-, dual-, and multi-indenter analyses, with the goal of significantly reducing the required number of high-fidelity datasets to achieve a chosen level of accuracy, and to significantly improve the accuracy and reliability of the mechanical properties extracted from depth-sensing instrumented indentation. Specifically, the methods outlined here, are shown to 1) significantly reduce the number of high-fidelity datasets needed to achieve a chosen level of accuracy; 2) utilize previously established physical and scaling laws to improve the accuracy and training efficiency; and 3) integrate simulation data and experimental data (i.e., data fusion) for training and significantly reducing material and/or experimental setup related systematic errors.

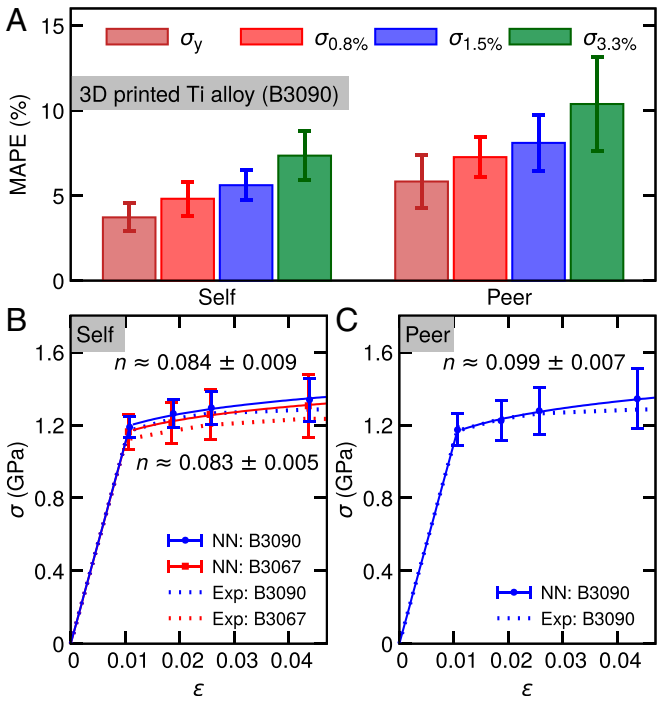

Fig. 9. Inverse analysis results of hardening exponent for two 3D printed Ti-6Al-4V alloys B3067 and B3090. (*A*) Mean average percentage error of σ_y, $\sigma_{0.8\%}$, $\sigma_{1.5\%}$, and $\sigma_{3.3\%}$ for B3090 predicted by NNs trained by 2D axisymmetric FEM data (low fidelity) with 3D Berkovich FEM data and five randomly picked Self and Peer experimental indentation curves (high fidelity). (*B* and *C*) The hardening exponent is obtained by least-squares fitting of σ_y, $\sigma_{0.8\%}$, $\sigma_{1.5\%}$, and $\sigma_{3.3\%}$ for (*B*) Self and (*C*) Peer experimental indentation curves. The experimentally extracted best-fit hardening exponent is $n = 0.068$ for both B3090 and B3067 uniaxial experiments, i.e., near zero low hardening. With additional experimental data added for training, the NNs predicts accurately the yield strength and low hardening behaviors. Here, the subscripts 0.8%, 1.5%, and 3.3% for σ represent plastic strains.

Our results are validated with independent experimental data and sources for different types of wrought aluminum and 3D printed titanium alloys.

In order to expedite the training of NNs, we have also developed a transfer learning technique, where the entire multifidelity network (both low- and high-fidelity subnetworks) is first trained using all of the 2D and 3D FEM data as the baseline training. This baseline training covers the material parameter space for the majority of engineering metals and alloys under an idealized testing condition. When given the additional experimental data for materials under a specific experimental setup, only the high-fidelity subnetwork needs to be further trained. The results in Fig. 10 show that we can first establish a comprehensive baseline training and then add additional case-specific training later for improved training efficiency and accumulated learning. With a small number of high-fidelity experimental data points added for training, significant improvements are achieved. This is due to the fact that, for a nominally homogeneous material, instrumented indentation experiments are known to produce highly repeatable force vs. penetration depth curves when using the same indenter instrument and the same experimental setup conditions. When we have a reliable method that can effectively learn and correct systematic errors, we can then use the method to calibrate the indenter and obtain accurate and reliable inverse analyses results. Additional discussion on the sensitivity of the inverse indentation problem in extracting plastic properties can be found in *SI Appendix*, Fig. S5.

There are several potentially appealing consequences of the results obtained in this work. 1) The approach described here provides unique pathways to extract critically needed information on mechanical properties, which cannot be easily obtained by other means, in a wide variety of engineering applications involving both structural and functional materials of different types and size scales. 2) With the cost effectiveness and sophistication of instrumented indentation, robotics, and computing tools, the present approaches can readily be incorporated in a wide variety of manufacturing settings (such as those involving 3D printing) for in situ and real-time estimation of material properties. 3) The approach is also highly adaptable and dynamic in that refinements in the choice of a particular DL approach can be made "on-the-fly" depending on the processing conditions, specimen geometry, material characteristics, speed of manufacturing, and the level of accuracy sought in the extracted values of properties. 4) The approaches described here can also be further enhanced, with appropriate modifications, to account for such factors as a) the buildup of residual stresses during the processing of the material, b) level of anisotropy in material properties, c) multicomponent architectures involving particle-reinforced, fiber-reinforced, or layered composite materials, and d) tailoring of surface and bulk properties through the deliberate introduction of structural, compositional, geometrical, and property gradients.

Methods

General Considerations. We implicitly utilize physically based scaling laws such as Kick's law (44) to simplify the problem and reduce data noise. For this purpose, instead of the common practice of directly using data points within the individual indentation curves for training, we choose key indentation parameters such as loading curvature *C*, initial unloading slope, $\frac{dP}{dh}\big|_{h_m}$, plastic work ratio, W_p/W_t, etc., for indentation inverse problem input and the

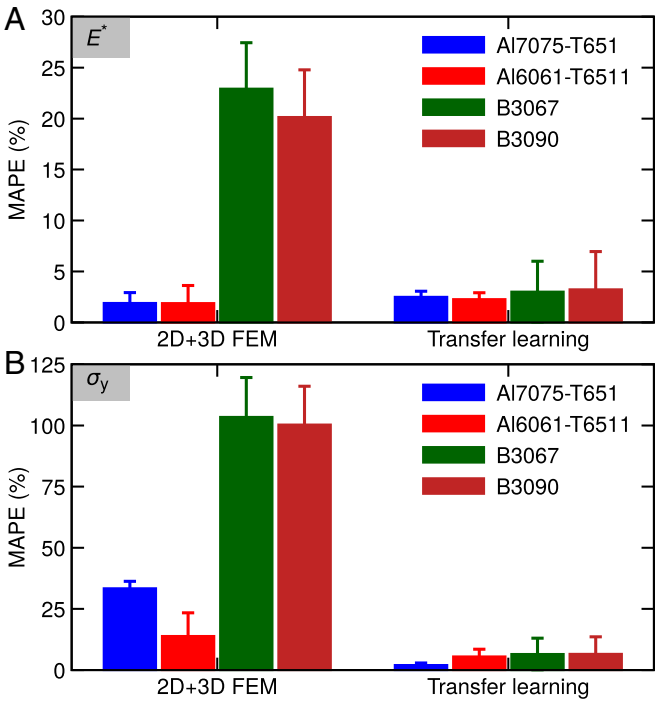

Fig. 10. Inverse analysis results of (*A*) E^* and (*B*) σ_y for NNs via transfer learning for two aluminum alloys Al6061-T6511 and Al7075-T651 and two 3D printed Ti-6Al-4V alloys B3067 and B3090. An MFNN is first trained on the dataset of the 2D FEM as the low-fidelity data and 3D FEM as the high-fidelity data (the results labeled as "2D + 3D FEM"). Next, the high-fidelity subnetwork is continued to be trained using three- and five-experiment data for aluminum alloys and 3D printed Ti-6Al-4V alloys, respectively, which the low-fidelity subnetwork does not change (the results labeled "Transfer learning").

power-law elastoplastic material parameters Young's modulus, E (or reduced modulus, E^*), yield strength, σ_y, hardening exponent, n, etc. (defined in equations 1–4 in *SI Appendix*, SI text) as the output.

On the other hand, since different datasets are obtained for different maximum depth of indenter penetration into the substrate, h_m, we apply the scaling law (established through dimensional analysis in ref. 5) between $\left.\frac{dP}{dh}\right|_{h_m}$ and h_m:

$$\left.\frac{dP}{dh}\right|_{h_m} \propto h_m,$$

to scale all of the datasets with different h_m, thereby reducing the required amount of training data.

NN Architecture for Single Indentation and Dual/Multiple-Indentation Inverse Problems.

Single indenter inverse problem. For solving the single-indentation inverse problem, two fully connected NNs are trained separately to represent the mapping from (C, dP/dh, W_p/W_t) to E^* and σ_y, respectively. Each NN has three layers with 32 neurons per layer (Fig. 1*B*). The nonlinear activation function is chosen as the scaled exponential linear unit (SELU) (45). To avoid overfitting, regularization can be applied to limit the freedom of the model by adding a penalty on the involved model parameters. Here, we use the standard L_2 regularization (46) with a strength of 0.01. Throughout our work, the level of accuracy in estimating any mechanical property is quantified by the MAPE (47). The NNs are optimized using the Adam optimizer (48) with learning rate 0.0001 for 30,000 steps.

Dual/multiple-indenter inverse problem. For solving the dual/multiple-indentation inverse problem, there exist different possibilities for selecting the input parameters. In the present study, we choose (C, dP/dh, W_p/W_t) extracted from indentation curves using the 70.3° conical tip and C from indentation curves using the 60° conical tip as the inputs of NNs. For solving the multiple-indentation inverse problem, we choose (C, dP/dh, W_p/W_t) extracted from indentation curves using the 70.3° conical tip and loading curvatures (C) from indentation curves using 50°, 60°, and 80° conical tips as the inputs of NNs. For the dual/multiple-indentation problem, the same NN architecture is applied as that is utilized in solving the single-indentation inverse problem (Fig. 1*B*), except that a faster learning rate of 0.001 is taken.

Experimental Method for Obtaining Indentation Datasets from 3D Printed Ti Alloys. Nanoindentation experiments were performed on samples (5 mm × 5 mm square cross-section and 10-mm height) that were electro-discharge-machined from larger 3D printed coupons with selected printing (laser melting) conditions (see ref. 42 for details on the printing conditions and postprinting heat treatment for B3067, B3090, B6067, B6090, S3067, and S6067 samples). The cut samples were first polished using emery paper (particle size, 9 μm) and then electropolished before indented using a Hysitron Triboindeter (Hysitron) equipped with a Berkovich diamond indenter tip in load control mode, under the following experimental conditions: peak load, 9 mN; loading rate, 0.9 mN/s; hold time at the peak load, 5 s; unloading rate, 1.8 mN/s. A total of 144 nanoindentations were performed on each sample over a 360 × 360-μm^2 area, with a distance of 30 μm (in both x and y directions) between two adjacent indents. Before each set of nanoindentation experiments, the tip was calibrated using a standard reference sample of fused quartz. Load, P, vs. depth of penetration, h, data were recorded.

MFNN and Unique Inverse Problem Setups.

Residual-based MFNN. For the MFNN, we propose a new residual-based MFNN (Fig. 1*D*), extending the method first developed by Meng and Karniadakis (34) (Fig. 1*C*). As shown in Fig. 1 *C* and *D*, the low-fidelity function y_L is the output of a neural network $\mathrm{NN_L}$ with input x. In ref. 34, the high-fidelity y_H is a weighted summation of a linear function and a nonlinear function (Fig. 1*C*):

$$y_H(x) = \alpha_1 f_{\mathrm{linear}}(x, y_L(x)) + \alpha_2 f_{\mathrm{nonlinear}}(x, y_L(x)),$$

where $f_{\mathrm{linear}}(x, y_L)$ and $f_{\mathrm{nonlinear}}(x, y_L)$ are linear and nonlinear functions of inputs (x, y_L), respectively. In particular, $f_{\mathrm{nonlinear}}(x, y_L)$ is another NN, represented by $\mathrm{NN_H}$ in Fig. 1*C*, while $f_{\mathrm{linear}}(x, y_L)$ is a single neuron with no activation function. In addition to the parameters in $f_{\mathrm{linear}}(x, y_L)$ and $f_{\mathrm{nonlinear}}(x, y_L)$, α_1 and α_2 are also two additional parameters to be trained.

We extended this method by adding an extra connection from y_L to y_H, and adopting a specific form of α_1 and α_2 to correlate the high- and low-fidelity data (Fig. 1*D*):

$$y_H = \alpha_L y_L + \epsilon(\tanh\alpha_1 \cdot f_{\mathrm{linear}}(x, y_L) + \tanh\alpha_2 \cdot f_{\mathrm{nonlinear}}(x, y_L)),$$

where α_1 and α_2 are two parameters to be learned. The coefficient α_L represents the ratio of the high-fidelity to low-fidelity outputs, and ϵ represents the ratio of the residual to the high-fidelity output. In principle, α_L can also be a learnable parameter as α_1 and α_2, but here we choose α_L to be 1, because in the indentation problems we considered y_L is usually of the same order of y_H, i.e., the residual $y_H - y_L$ is much smaller than y_L and y_H. For the same reason, we choose ϵ as a small positive number to be 0.1. The network prediction is not very sensitive to the values of α_L and ϵ, if their magnitudes are chosen correctly. However, the network may be trained to a wrong state if the values are incorrectly selected. In addition, at the beginning of training, we initialize α_1 and α_2 to be 0, such that the learning of y_H starts from y_L.

Our proposed MFNN makes the training process more stable and yields better accuracy compared to the original MFNN. The reason is that it is much easier for $f_{\mathrm{linear}}(x, y_L)$ and $f_{\mathrm{nonlinear}}(x, y_L)$ to learn the residual $y_H - y_L$ than to learn y_H directly. This residual approach was first proposed with the name "ResNet" (49), and since then it has been widely used in many computer vision tasks.

We follow three multifidelity ML approaches in the present study. All versions of MFNNs are implemented in DeepXDE (50), a user-friendly Python library designed for scientific ML.

Approach 1: Integrating data generated from fitting functions (low fidelity) and FEM simulation data (high fidelity). We first test the proposed multifidelity approach using the conical single indentation data for materials with $n \leq 0.3$ (still covering the material parameter space for majority of engineering metals). The low-fidelity dataset is generated by using the fitting functions from ref. 5, while the high-fidelity dataset is based on the 2D axisymmetric finite-element simulations.

Approach 2: Solving inverse 3D indentation problems (e.g., with Berkovich tip) by integrating 2D axisymmetric FEM data (low fidelity) with 3D FEM data (high fidelity). Traditionally, algorithms based on conical indentation finite element results were used for obtaining approximate solutions of Vickers or Berkovich 3D indentation problems (5, 6, 9, 18–20). Here, we integrate the low-cost 2D axisymmetric finite-element data (low fidelity) with a limited number of 3D finite-element simulation data (high fidelity) to solve the Berkovich indentation inverse problem.

Approach 3: Learning and correcting material- and/or setup-specific systematic errors by including a few experimental data as part of the high-fidelity training data. In instrumented-indentation experiments, material-specific (e.g., for a material that is not well represented by power-law hardening) and/or equipment-specific (e.g., nonlinear machine compliance) systematic errors can be significantly enlarged when performing inverse analyses. We attempt to overcome this issue by adding a few experimental data as part of the high-fidelity training data in approach 2. Specifically, the experimental data added for training can come from the same material using the same experimental setup or from a different calibration material tested under the same experimental conditions.

Data Availability. The code and related input data have been deposited in GitHub at https://github.com/lululxvi/deep-learning-for-indentation. All other data are included in the manuscript and *SI Appendix*.

ACKNOWLEDGMENTS. G.E.K. acknowledges support by the Army Research Laboratory (W911NF-12-2-0023) and the Department of Energy (DE-SC0019453). S.S. acknowledges Nanyang Technological University, Singapore, for support through the Distinguished University Professorship.

1. W. C. Oliver, G. M. Pharr, An improved technique for determining hardness and elastic modulus using load and displacement sensing indentation experiments. *J. Mater. Res.* **7**, 1564–1583 (1992).
2. S. Suresh, A. E. Giannakopoulos, A new method for estimating residual stresses by instrumented sharp indentation. *Acta Mater.* **46**, 5755–5767 (1998).
3. Y. T. Cheng, C. M. Cheng, Relationships between hardness, elastic modulus, and the work of indentation. *Appl. Phys. Lett.* **73**, 614–616 (1998).
4. A. E. Giannakopoulos, S. Suresh, Determination of elastoplastic properties by instrumented sharp indentation. *Scr. Mater.* **40**, 1191–1198 (1999).
5. M. Dao, N. Chollacoop, K. J. Van Vliet, T. A. Venkatesh, S. Suresh, Computational modeling of the forward and reverse problems in instrumented sharp indentation. *Acta Mater.* **49**, 3899–3918 (2001).
6. N. Chollacoop, M. Dao, S. Suresh, Depth-sensing instrumented indentation with dual sharp indenters. *Acta Mater.* **51**, 3713–3729 (2003).

7. W. C. Oliver, G. M. Pharr, Measurement of hardness and elastic modulus by instrumented indentation: Advances in understanding and refinements to methodology. *J. Mater. Res.* **19**, 3–20 (2004).
8. A. Gouldstone *et al*., Indentation across size scales and disciplines: Recent developments in experimentation and modeling. *Acta Mater.* **55**, 4015–4039 (2007).
9. H. Z. Lan, T. A. Venkatesh, Determination of the elastic and plastic properties of materials through instrumented indentation with reduced sensitivity. *Acta Mater.* **55**, 2025–2041 (2007).
10. O. Jorgensen, A. E. Giannakopoulos, S. Suresh, Spherical indentation of composite laminates with controlled gradients in elastic anisotropy. *Int. J. Solids Struct.* **35**, 5097–5113 (1998).
11. S. Suresh, Graded materials for resistance to contact deformation and damage. *Science* **292**, 2447–2451 (2001).
12. I. S. Choi, M. Dao, S. Suresh, Mechanics of indentation of plastically graded materials—I: Analysis. *J. Mech. Phys. Solids* **56**, 157–171 (2008).
13. S. Sridhar, A. E. Giannakopoulos, S. Suresh, U. Ramamurty, Electrical response during indentation of piezoelectric materials: A new method for material characterization. *J. Appl. Phys.* **85**, 380–387 (1999).
14. A. Saigal, A. E. Giannakopoulos, H. E. Pettermann, S. Suresh, Electrical response during indentation of a 1-3 piezoelectric ceramic-polymer composite. *J. Appl. Phys.* **86**, 603–606 (1999).
15. D. Tabor, *The Hardness of Metals* (Clarendon Press, Oxford, UK, 1951).
16. P. Zhang, S. X. Li, Z. F. Zhang, General relationship between strength and hardness. *Mater. Sci. Eng. A* **529**, 62–73 (2011).
17. Y. T. Cheng, C. M. Cheng, Scaling, dimensional analysis, and indentation measurements. *Mater. Sci. Eng.* **44**, 91–149 (2004).
18. J. L. Bucaille, S. Stauss, E. Felder, J. Michler, Determination of plastic properties of metals by instrumented indentation using different sharp indenters. *Acta Mater.* **51**, 1663–1678 (2003).
19. Y. P. Cao, J. Lu, Depth-sensing instrumented indentation with dual sharp indenters: Stability analysis and corresponding regularization schemes. *Acta Mater.* **52**, 1143–1153 (2004).
20. L. G. Wang, M. Ganor, S. I. Rokhlin, Inverse scaling functions in nanoindentation with sharp indenters: Determination of material properties. *J. Mater. Res.* **20**, 987–1001 (2005).
21. D. J. Ma, C. W. Ong, J. Lu, J. W. He, Methodology for the evaluation of yield strength and hardening behavior of metallic materials by indentation with spherical tip. *J. Appl. Phys.* **94**, 288–294 (2003).
22. Y. P. Cao, J. Lu, A new method to extract the plastic properties of metal materials from an instrumented spherical indentation loading curve. *Acta Mater.* **52**, 4023–4032 (2004).
23. W. Y. Ni, Y. T. Cheng, C. M. Cheng, D. S. Grummon, An energy-based method for analyzing instrumented spherical indentation experiments. *J. Mater. Res.* **19**, 149–157 (2004).
24. M. Q. Le, Material characterization by instrumented spherical indentation. *Mech. Mater.* **46**, 42–56 (2012).
25. Y. Z. Li, P. Stevens, M. C. Sun, C. Q. Zhang, W. Wang, Improvement of predicting mechanical properties from spherical indentation test. *Int. J. Mech. Sci.* **117**, 182–196 (2016).
26. Y. Kassahun *et al*., Surgical robotics beyond enhanced dexterity instrumentation: A survey of machine learning techniques and their role in intelligent and autonomous surgical actions. *Int. J. Comput. Assist. Radiol. Surg.* **11**, 553–568 (2016).
27. B. F. Spencer, V. Hoskere, Y. Narazaki, Advances in computer vision-based civil infrastructure inspection and monitoring. *Engineering* **5**, 199–222 (2019).
28. T. Young, D. Hazarika, S. Poria, E. Cambria, Recent trends in deep learning based natural language processing. *IEEE Comput. Intell. Mag.* **13**, 55–75 (2018).
29. B. Sanchez-Lengeling, A. Aspuru-Guzik, Inverse molecular design using machine learning: Generative models for matter engineering. *Science* **361**, 360–365 (2018).
30. A. Esteva *et al*., A guide to deep learning in healthcare. *Nat. Med.* **25**, 24–29 (2019).
31. Z. Shi *et al*., Deep elastic strain engineering of bandgap through machine learning. *Proc. Natl. Acad. Sci. U.S.A.* **116**, 4117–4122 (2019).
32. M. C. Kennedy, A. O'Hagan, Predicting the output from a complex computer code when fast approximations are available. *Biometrika* **87**, 1–13 (2000).
33. A. Forrester, A. Sobester, A. Keane, *Engineering Design via Surrogate Modelling: A Practical Guide* (Wiley, 2008).
34. X. Meng, G. E. Karniadakis, A composite neural network that learns from multi-fidelity data: Application to function approximation and inverse PDE problems. *J. Comput. Phys.* **401**, 109020 (2020).
35. N. Huber, A. Konstantinidis, C. Tsakmakis, Determination of Poisson's ratio by spherical indentation using neural networks—Part I: Theory. *J. Appl. Mech.* **68**, 218–223 (2001).
36. N. Huber, C. Tsakmakis, Determination of Poisson's ratio by spherical indentation using neural networks—Part II: Identification method. *J. Appl. Mech.* **68**, 224–229 (2001).
37. E. Tyulyukovskiy, N. Huber, Identification of viscoplastic material parameters from spherical indentation data: Part I. Neural networks. *J. Mater. Res.* **21**, 664–676 (2006).
38. A. H. Mahmoudi, S. H. Nourbakhsh, "A neural networks approach to characterize material properties using the spherical indentation test" in *11th International Conference on the Mechanical Behavior of Materials*, M. Guagliano, L. Vergani, Eds. *Procedia Engineering* 10, 3062–3067 (2011).
39. R. Haj-Ali, H.-K. Kim, S. W. Koh, A. Saxena, R. Tummala, Nonlinear constitutive models from nanoindentation tests using artificial neural networks. *Int. J. Plast.* **24**, 371–396 (2008).
40. H. Li *et al*., Identification of material properties using nanoindentation and surrogate modeling. *Int. J. Solids Struct.* **81**, 151–159 (2016).
41. Y. Zhang, J. D. Hart, A. Needleman, Identification of plastic properties from conical indentation using a bayesian-type statistical approach. *J. Appl. Mech.* **86**, 011002 (2019).
42. P. Kumar, O. Prakash, U. Ramamurty, Micro-and meso-structures and their influence on mechanical properties of selectively laser melted Ti-6Al-4V. *Acta Mater.* **154**, 246–260 (2018).
43. I. Choi, O. Kraft, R. Schwaiger, Validity of the reduced modulus concept to describe indentation loading response for elastoplastic materials with sharp indenters. *J. Mater. Res.* **24**, 998–1006 (2009).
44. K. L. Johnson, *Contact Mechanics* (Cambridge University Press, Cambridge, UK, 1985).
45. G. Klambauer, T. Unterthiner, A. Mayr, S. Hochreiter, "Self-normalizing neural networks" in *Advances in Neural Information Processing Systems 30*, I. Guyon *et al*., Eds. (Advances in Neural Information Processing Systems, Curran Associates, Montreal, QC, Canada, 2017), vol. 30, pp. 972–981.
46. A. Y. Ng, "Feature selection, L_1 vs. L_2 regularization, and rotational invariance" in *Proceedings of the Twenty-First International Conference on Machine Learning* (ACM, Banff, AB, Canada, 2004), p. 78.
47. A. De Myttenaere, B. Golden, B. Le Grand, F. Rossi, Mean absolute percentage error for regression models. *Neurocomputing* **192**, 38–48 (2016).
48. D. P. Kingma, J. Ba, Adam: A method for stochastic optimization. arXiv:1412.6980 (30 January 2017).
49. K. M. He, X. Y. Zhang, S. Q. Ren, J. Sun, "Deep residual learning for image recognition" in *Proceedings of the IEEE Conference on Computer Vision and Pattern Recognition* (IEEE, 2016), pp. 770–778.
50. L. Lu, X. Meng, Z. Mao, G. E. Karniadakis, DeepXDE: A deep learning library for solving differential equations. arXiv:1907.04502 (10 July 2019).